The effects of synthetic wollastonite microfibers on PVA fiber-reinforced engineered geopolymer composites

⬥H.Ö. Öz[a], ⬥M. Güneş[b]✉

a. Department of Civil Engineering, Niğde Ömer Halisdemir University, (Niğde, Türkiye)
b. Department of Civil Engineering, Nevşehir Hacı Bektaş Veli University, (Nevşehir, Türkiye)
✉: muhammet.gunes@nevsehir.edu.tr

ABSTRACT: In this study, first, synthetic wollastonite microfiber (SWM) with a high aspect ratio (44:1) was produced with a special three-stage production method. Then, fly ash and ground granulated blast furnace slag-based engineered geopolymer composites (FA+GGBFS-based EGCs) were developed. SWM was used in different proportions instead of FA. The compressive strength of EGCs, changed in the range of 88.1–111.1 and 95.1–122.6 MPa at 7 and 28 days, respectively. Additionally, EGCs containing 6% SWM performed the best, considering both ''increasing deformation capacity'' and ''maintaining the bearing strength by fiber bridging after crack'', since they acted like a fiber owing to the acicular particle structure of SWM. Moreover, it can be said that the presence of the SWM mineral in the pore system, ensured pore discontinuities in the matrix because of its acicular particle structure. Consequently, the mechanical, durability and dimensional stability properties of EGCs improved with SWM.

KEY WORDS: EGC; Synthetic wollastonite microfiber; Mechanical, durability and dimensional stability properties; Freeze-thaw resistance; TGA/DTA.

Citation/Citar como: Öz HÖ, Güneş M. 2024. The effects of synthetic wollastonite microfibers on PVA fiber-reinforced engineered geopolymer composites. Mater. Construcc. 74(354):e345. https://doi.org/10.3989/mc.2024.363423.

RESUMEN: *Efectos de microfibras de wollastonita sintética en compuestos de geopolímeros ingenieriles reforzados con fibras de PVA.* En este estudio, en primer lugar, se produjeron microfibras sintéticas de wollastonita (MSW) con una elevada relación de aspecto (44:1) mediante un método especial de producción en tres etapas. A continuación, se desarrollaron compuestos geopoliméricos de ingeniería basados en cenizas volantes y escoria de alto horno granulada molida (CGI basados en CV+EGMAH). Se utilizó MSW en diferentes proporciones en lugar de CV. La resistencia a la compresión de los CGI, varió en el rango de 88,1–111,1 y 95,1–122,6 MPa a los 7 y 28 días, respectivamente. Además, los CGIs que contenían un 6% de MSW obtuvieron los mejores resultados, considerando tanto el "aumento de la capacidad de deformación" como el "mantenimiento de la resistencia a la compresión mediante la formación de puentes de fibras después de la fisuración", ya que actuaron como una fibra debido a la estructura de partículas aciculares del MSW. Además, puede decirse que la presencia del mineral MSW en el sistema de poros, aseguró discontinuidades de poros en la matriz debido a su estructura de partícula acicular. En consecuencia, las propiedades mecánicas, de durabilidad y de estabilidad dimensional de los CGI mejoraron con el MSW.

PALABRAS CLAVE: CGI; Microfibra sintética de wollastonita; Propiedades mecánicas, de durabilidad y estabilidad dimensional; Resistencia al hielo-deshielo; TGA/DTA.

1. INTRODUCTION

Nowadays, sustainable developments for environmental protection have drawn attention to the construction industry, particularly with regard to the energy consumption and carbon footprint of cement production. Hence, finding an alternative material for cement-based composites to meet high-performance characteristics and environmental protection measures is a challenge of current research (1, 2). Although conventional concrete is the most commonly used construction and building material in the world, it is brittle and prone to cracking with a low tensile strain ability of only about 0.01% (3, 4).

Engineered cementitious composites (ECCs), known as strain-hardening cementitious composites, are a novel type of ultra-ductile fiber-reinforced concrete developed in the 1990s to improve especially the ductility and low tensile strength of concrete (5, 6). One of the most significant properties of ECCs can be defined as the formation of multiple micro-cracks by retarding the onset and further propagation of cracking and controlling crack widths (<100 μm) (7, 8). Owing to their micro-mechanical design theory, ECCs have been developed with a moderate PVA fiber volume of 2% to ensure high damage tolerance, high tensile strength and self-healing ability with multiple micro-cracking behavior (6). However, ECC mixes are costly and contain about 2–3 times higher cement content than conventional concrete due to a lower aggregate content, which would aggravate the current situation since cement production is responsible for approximately 8% of CO_2 emissions in the world (3, 4, 9, 10). Therefore, it is extremely important to make various attempts in order to discover alternative binders/materials for/instead of ECCs. Geopolymers, a kind of environmental inorganic cementitious material, are produced from a chemical reaction between alkaline activators and aluminosilicate source materials (11-13). Since fly ash (FA) has a low water demand due to its spherical shape for high workability, it is the main source of aluminosilicates required for geopolymer production. In the presence of an alkaline solution, FA forms highly cross-linked N-A-S-H gels by geopolymerization that bonds the particles via hardening (14, 15). Although geopolymers have advantages over cement, such as a simple manufacturing process that requires better mechanical characteristics and lower energy consumption in different situations (16, 17), they exhibit a brittle behavior. In this case, the mechanism of fiber reinforcement controls the crack propagation through the bridging effect of fiber. It changes the post-cracking behavior of the composite from a brittle format to a ductile mode because of its improved energy dissipation capacity (18). Thus, the use of geopolymer binders as a matrix composite by taking advantage of ECCs leads to new attempts to develop engineered geopolymer

composites (EGCs) as a type of up-and-coming substitute for ECC (19). EGCs are developed from geopolymers by incorporating PVA fibers, basalt fibers, and steel fibers into the geopolymer to control cracking. EGCs are characterized by multiple simultaneous fractures under tensile action. Their other advantages include high ultimate tensile strain and crack resistance and broad application prospects in building engineering and structural reinforcement and repair (20). Moreover, it has been reported that several EGCs exhibit similar mechanical properties to conventional ECCs with high ductility (18-22). Similar to ECCs, EGCs contain randomly deployed short fibers at a rate usually not higher than 2.0% (23). It has been concluded that by incorporating a 2% PVA fiber volume into EGC, its compressive strength, flexural performance, and fracture toughness, along with abrasion resistance, can be considerably enhanced, indicating typical strain hardening with multiple micro-cracking behavior (7, 8, 15, 24). However, the use of FA in EGC has limitations due to its low reactivity, which often leads to slow setting and does not meet the requirements of different situations. The low reactivity of FA can be overcome by substituting FA for waste minerals such as ground granulated blast furnace slag (GGBFS) in EGC mixes. Moreover, the high CaO content, high reactivity, and cementitious properties of GGBFS result in the early age strength development and better setting characteristics of geopolymers in comparison with FA (25-27). Additionally, the geopolymerization of binders may lead to the regulation of C–S–H/C-A-S-H gel as well as N-A-S-H gel (FA-based geopolymer gel) via the addition of GGBFS, thus further improving the mechanical and microstructural properties (28, 29). However, along with the aforementioned advantages, geopolymers produced with GGBFS have cracking problems in oven curing and, therefore, generally gain strength in ambient curing. This results in the inability to fully utilize the high reactivity of CaO (27). Hence, Coppala et al. (30) conducted a study to increase the rate at which CaO in GGBFS gains strength without heat cracking, opposite to ambient curing. The study by Coppala et al. (30) also emphasized that the steam curing of FA+GGBFS-based geopolymer at 40 °C/60 °C enhanced the higher early compressive strength compared to ambient curing at particularly high GGBFS/FA ratios.

Unlike fiber fillers, powder fillers can be added to the geopolymer matrix composite to improve its strength properties (31). Wollastonite (calcium meta silicate) is a naturally occurring white mineral with needle-like crystals and an acicular particle shape or fiber morphology, which has a particle size similar to that of cement (32, 33). It exhibits inert characteristics in the reaction so that it does not react with other components. Thus, this material has been used as an alternative microfiber for cement and

geopolymer-based materials due to its fineness and chemical composition (33). The study by Archez et al. (34) reported that wollastonite enhanced the viscosity and mechanical performance of geopolymer while decreasing its workability by providing a better solution of metakaolin. Soliman and Nehdi (35) observed a 12% decrease in workability with the addition of 17% wollastonite because of the interlocking effect of wollastonite needles. Likewise, Vickers et al. (23) obtained a 53% decrease in flowability with the addition of 13% wollastonite. Hemalatha and Ramujee (32) observed an 18–20% increment in compressive strength with the addition of wollastonite. Silva and Thaumaturgo (36) showed that fracture toughness was successfully improved by adding natural wollastonite microfibers (NWMs) to the geopolymer matrix. Furthermore, it was noted that NWMs were compatible with the high pH levels utilized in geopolymer matrix synthesis with a denser interfacial transition zone (37). Nurjaya et al. (31) reported that wollastonite microfibers slightly increased the flexural strength of the geopolymer matrix since they produced only a very small bridging effect. In addition to NWMs, synthetic wollastonite microfibers (SWMs) can be synthesized from calcite and silica sand in a different way from the literature (6, 38). Compared to NWMs, SWMs have an acicular structure that is more homogeneously distributed in the whole mass, which improves the mechanical and durability properties of cement composites (38, 39). The effects of SWM on the properties of cement/geopolymer composites have rarely been studied. Öz and Güneş (38) reported that the mechanical performance of high-performance cement mortar improved up to 9 wt% of SWM and decreased beyond this substitution amount (40). Yücel et al. (6) developed two types of SWMs and used SWMs instead of cement+FA, reporting that the bearing capacity and deformation capacity performances of ECCs improved with the increasing aspect ratio of SWM. However, in the study by Öz and Ünsal (41), SWM was used as 0, 4, 8, and 12% by weight of binder in the production of self-compacting geopolymer mortar. 28.9 MPa was determined to be the highest compressive strength for self-compacting geopolymer mortar designed with an alkali activator ratio of 1.5 and an 8% replacement level of SWM cured at 100 °C, while the highest flexural strength value was obtained as 6.5 MPa for self-compacting geopolymer mortar designed with a temperature of 80 °C, 12% substitution level of SWM, and an alkali activator ratio of 2.

To the best of the authors' knowledge, there is no study on EGC design incorporating NWM or SWM. The original idea was to take advantage of SWM's ability to behave like a fiber due to its needle-like particle structure. Therefore, this study aimed to investigate the possible effects of SWM on EGCs. The first section of the study covered the production of SWM with a high aspect ratio from calcite and silica sand in a different way from the literature. Then, EGCs were produced with SWM instead of FA. After observing the fresh properties, the mechanical, durability, and dimensional stability properties of EGCs cured in water at 60 °C until the test age were investigated.

2. EXPERIMENTAL STUDY

2.1. The production process of SWM

Three different methods are employed to produce synthetic wollastonite. These methods are the wet method, the solid-state reaction method, and the liquid-phase reaction method. All of the aforesaid methods are suitable to achieve a limited aspect ratio. Therefore, special methods should be developed to achieve the highest aspect ratio (6, 39). The production of SWM with an extremely high maximum aspect ratio (44:1) developed by utilizing natural materials is described as follows: At the first step of the three-step production process, 1:1 mol CaO and SiO_2 (56.08 and 60.08 g) and water (116.16 g) equal to the total weight of these two raw materials were mixed in a ball mill at 250 rpm for 30 minutes. After this step, called the mechanochemical process, the mixture placed in Teflon was kept in the oven at 200 °C and a pressure created by the autoclave for two days. At the second step, defined as the hydrothermal autoclave process, the tobermorite mineral was obtained. The tobermorite mineral, which was dehumidified at 100 °C for 24 hours, was subjected to pre-milling. Afterward, this mineral was kept in the ash oven at 1000 °C for 1 hour. Thus, in the third and last step, defined as the sintering process, SWM was obtained. After final milling, this material was used in FA+GGBFS-based EGC instead of FA.

2.2. XRD, SEM, and XRF analysis of SWMs

Figure 1 presents the XRD peak changes of NWM and SWM. When the XRD peaks of these materials were examined, it was determined that the peaks of SWM were largely similar to natural wollastonite peaks. In particular, it can be said that the peaks at the 20-30 angular position [°2θ] levels, where peaks with high intensity occur, matched natural wollastonite peaks. The SEM images in Figure 2(a-b) show that almost all of the SWM particles had an acicular particle structure. In the SEM image in Figure 2(b), the SWM particle with the maximum aspect ratio was detected, and the maximum aspect ratio of SWM was determined as 44:1 using Pa 1/Pa 2 (4153 mm/94.26 nm). In light of the literature's definition of a high aspect ratio as 20:1 (6, 38, 41), it is

obvious that SWM with an extremely high maximum aspect ratio was developed. Table 1 lists the CaO and SiO$_2$ contents of SWM and NWM in different countries. It is seen that the CaO and SiO$_2$ contents of natural wollastonite vary between 42-50% and 46-55%, respectively, and these values for SWM are 45.74% and 50.71%, respectively. Therefore, XRD, SEM and XRF findings proved that this product, developed with a special technique, was wollastonite.
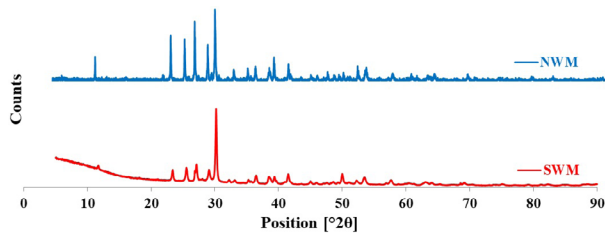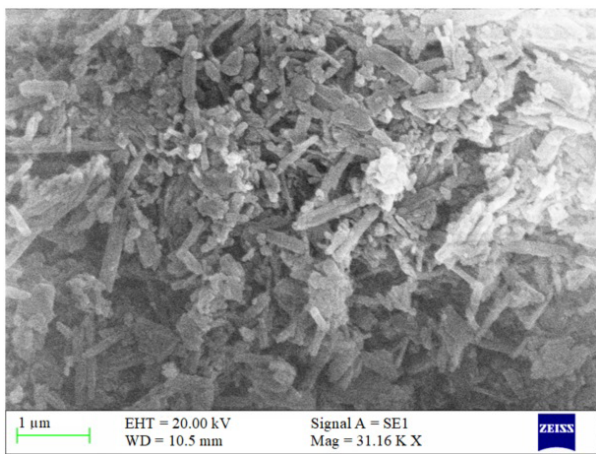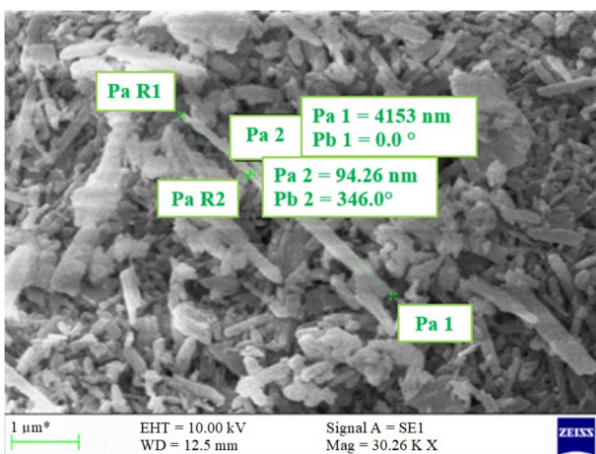
TABLE 1. CaO and SiO$_2$ contents of SWM and wollastonite in different countries.

Chemical Analysis (%)	SWM	Finland	USA	India	Kenya	Mexico	China
CaO	45.74	45	47	48	42	47	43-50
SiO$_2$	50.71	52	51	49	55	52	46-53

FIGURE 1. XRD analysis of NWM and SWM.

2.3. Materials

FA, GGBFS, NaOH, Na$_2$SiO$_3$, extra water, and PVA fiber were used in the design of the FA+GG-BFS-based control EGC mix (SWM0). SWM was utilized at the ratios of 3%, 6%, and 9% instead of FA. Figure 3 shows the particle size distributions of FA, GGBFS, and SWM. Table 2 contains the physical properties and chemical compositions of these materials. Na$_2$SiO$_3$ and 13 mol NaOH were used as alkali activators in the design of EGC mixes. Na$_2$SiO$_3$ (water glass), with a specific gravity of 1.399, was purchased in liquid form from the manufacturer. A liquid Na$_2$SiO$_3$ solution, with a SiO$_2$/Na$_2$O molar ratio (module of Na$_2$SiO$_3$) of 2.5, was produced from 38.5% solids and 61.5% water (H$_2$O). The solid part of the Na$_2$SiO$_3$ alkaline activator contains 27.56% SiO$_2$ and 10.94% Na$_2$O oxide. For composites' homogeneity, a fiber content of 2% by volume in excess of the calculated critical fiber content has been typically used in the mix design. The surface of the PVA fiber was coated with hydrophobic oil (1.2% by weight) to reduce the fiber/matrix interface bond strength. These decisions were made through ECC micromechanics material design theory and have been experimentally demonstrated to produce good ECC properties in previous research (42, 43). Therefore, PVA fiber was used as 2% by volume in EGCs.

(a)

(b)

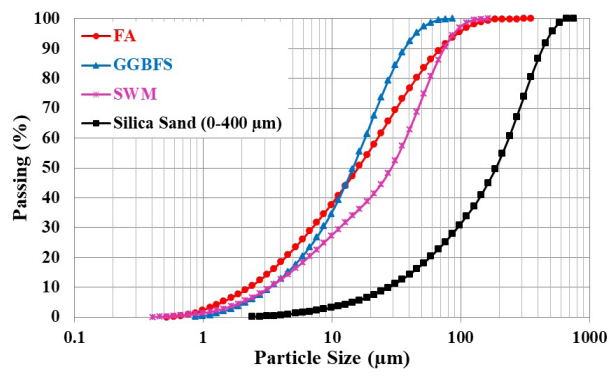**FIGURE 2.** (a) SEM image of SWM and the XRF analysis of SWM and NWM, (b) The determination of the maximum aspect ratio of SWM.

(b)

FIGURE 3. Particle size distributions of the materials used in the production of EGCs.

TABLE 2. Physical and chemical properties of FA, GGBFS, and SWM.

Chemical Analysis (%)	FA	GGBFS	SWM
CaO	1.47	38.83	45.74
SiO_2	61.25	36.82	50.71
Al_2O_3	22.19	13.31	0.24
Fe_2O_3	7.02	0.70	0.10
MgO	1.70	5.65	0.87
SO_3	0.06	0.50	0.34
K_2O	2.34	0.75	0.01
Na_2O	0.27	-	-
TiO_2	0.90	-	0.03
Physical properties	FA	GGBFS	SWM
Loss of Ignition	2.60	1.92	2.00
Specific Gravity	2.31	2.89	2.87

2.4. EGC mixing proportions and production procedure

The pseudo strain-hardening criteria used in the micromechanical model by Li and Leung (44) have been adopted for ECC design following a J-integral energy approach suggested by Marshall and Cox (45). Previous studies on EGCs have used the micromechanical model developed by Li et al. (44, 46), providing a solid theoretical design basis (47, 48). Despite the outstanding performance of EGCs in previous studies, challenges still exist regarding the mixture design of EGCs, which includes even more factors to be considered in comparison with the traditional EGC design (21). However, most studies on EGCs used the model in question mainly on already developed mixes to explain the origin of strain-hardening behavior and sometimes for optimization purposes (49). Thus, in line with the literature, the origin point of the matrix for EGC design is based on a PVA fiber-reinforced geopolymer composite that exhibits good deflection strain-hardening behavior (50). Furthermore, the consistent rheological properties of ECC and EGC mixes are among the most important for better fiber distribution and workability. In fact, the strain-hardening behavior of these composites depends on proper fiber distribution (51).

After the samples were poured into the mold, they were cured under laboratory conditions for 24 hours. Geopolymers produced with GGBFS have cracking problems in oven curing and, therefore, generally gain strength in ambient curing. This results in the inability to fully utilize the high reactivity of CaO (27). Therefore, FA+GGBFS-based EGCs, which were kept in the mold under laboratory conditions for 24 h immediately after production, were kept in water at 60 °C until the test age due to the improvement of the higher early compressive strength compared to ambient curing at particularly high GGBFS/FA ratios (30). In all FA+GGBFS-based EGC mixes, the ratio of Na_2SiO_3/NaOH was kept constant at 2.5, and the ratio of total alkali activator to total binder was 0.33. SWM was used instead of FA at the ratios of 3%, 6%, and 9%. Table 3 presents the mixing ratios of EGCs. The mixture nomenclature is very simple. Numbers 0, 3, 6, and 9 at the end of SWM indicate the percent by weight of SWM used instead of FA.

TABLE 3. Mixing proportions of EGCs (kg/m^3).

Mix ID	NaOH	Na_2SiO_3	FA	GGBFS	SWM	PVA	Extra Water
SWM0	124.6	311.6	785.2	523.5	0.0	26.0	157.1
SWM3	124.6	311.6	761.7	523.5	23.6	26.0	161.6
SWM6	124.6	311.6	738.1	523.5	47.1	26.0	168.1
SWM9	124.6	311.6	714.6	523.5	70.7	26.0	178.1

The same EGC mixtures were also produced without PVA.

2.5. Mini-slump

The workability properties of the fresh EGC matrices were determined with a mini-slump flow diameter. A truncated mini-slump cone with a height of 60 mm and a diameter of 70 mm at the top side and 100 mm at the bottom side was put on a smooth plate and then filled with ECC and EGC (without/with PVA fiber) and finally, lifted upward. When the composite flow was completed, the diameter of this shape was determined by two measurements. The deformations in the slump flow of EGCs were defined as the flow diameter when the mortar stopped flowing (6, 27).

2.6. Compressive strength

To define the compressive strength of EGCs, 50-mm cube samples were produced. A minimum of three compression cubes were utilized to determine the average strength with respect to ASTM C109 (52). The compressive test was carried out on a test device (Brand: Utest Materials Testing Equipment and Model: UTC-4731) with a loading speed of 0.9 kN/s and a capacity of 3000 kN.

2.7. Durability properties

Cylindrical samples with a length of 200 mm and a diameter of 100 mm were produced for the water

sorptivity test. The pieces with a length of 50 mm and a diameter of 100 mm cut from these samples were utilized to obtain three samples for each test age. Figure 4(a) shows the application of this test. The samples that arrived on the test day were kept in an oven at 50±5 °C. One of the two surfaces of the samples was chosen to allow water absorption, and the side of the selected surface was covered with silicone to prevent water permeability. After being weighed as dry weight, the samples were put in a tiny ball pool with a thin water layer of 5 mm according to ASTM C1585 standard (53). The samples' weights were measured at certain minutes after drying the wet surfaces with a dry cloth. Therefore, the water sorptivity coefficient of the samples was calculated by the amount of water absorbed over time per unit cross-sectional area. According to the test procedure, results were calculated with the determined average of the three samples' data using the equation below:

$$I = S^I \sqrt{t} \qquad [1]$$

where S^I: sorptivity (mm/min$^{0.5}$), I: cumulative infiltration (mm), and t: time (min).

The rapid chloride permeability test was performed in accordance with ASTM C1202 (54) on three discs with a height of 50 mm and a diameter of 100 mm, cut from a Ø150 300 mm cylinder. After curing, the samples were kept in a vacuum for 2 hours. The samples, whose vacuum process was completed, were placed in the test device with 3% NaCl on one side and 0.3 M NaOH solution on the other side, as seen in Figure 4(b). The resistance to chlorine ion penetration of EGCs was determined by the charge passing through the composite according to ASTM C1202 (54). Thus, during the 6-hour experiment, the amount of electric current passing through the disk was recorded by applying a constant potential difference of 60 V. The test

results were evaluated by taking the average of the three EGC samples at 7 and 28 days.

The Cembureau method suggested by RILEM (55) was applied to measure the apparent gas permeability of EGCs at 7 and 28 days. Figure 4(c) displays the test setup. The test sample belonging to gas permeability was produced as a disc with a thickness of 50 mm and a diameter of 150 mm, cut from 300 mm thick and 150 mm diameter cylinder samples. On the test days, the samples were dried at 50±5 °C. Then, they were allowed to cool until ambient temperature was reached in a sealed container. Inlet gas pressures were applied as 150, 250, and 300 kPa. Oxygen gas was used to provide the permeating medium. Gas permeability coefficients were determined for each level of these gas pressures. As given by RILEM (55), the apparent gas permeability coefficient was determined by the average of coefficients. The coefficient can be determined by modified Darcy's equation (Equation [2]) as follows:

$$K_a = \frac{2P_2 Q L \mu}{A(P_1^2 - P_2^2)} \qquad [2]$$

where K_a: apparent gas permeability coefficient (m^2), P_1: inlet gas pressure (N/m^2), P_2: outlet gas pressure (N/m^2), A: cross-sectional area of the sample (m^2), Q: volume flow rate (m^3/s), L: height of the sample (m), and μ: viscosity of oxygen (2.02 x 10^{-5} N s/m^2). Three samples for each EGC mixture were tested, and the average of them was determined as K_a.

Freeze-thaw tests of EGC mixes were performed according to procedure A specified in ASTM C666 (56). Six 400x100x100 mm prisms for the freeze-thaw test were produced from each EGC mix. All samples were demolded at the age of 24 hours and in water at 60 °C for 13 days. After 14 days, three beams for each mix were placed in the freeze-thaw cabinet. Accordingly, the samples placed in the cabinet were left completely in water and exposed to 3-4 freeze-thaw cycles within
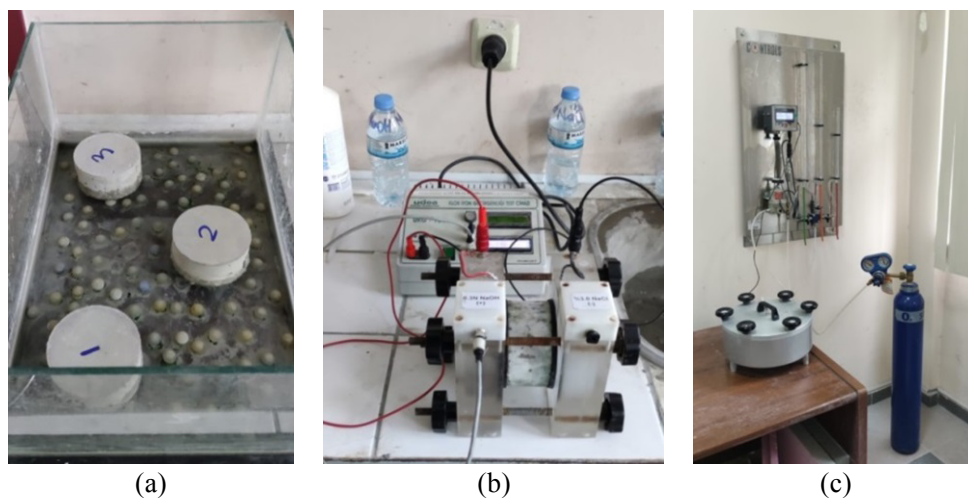

(a)　　　　　　　　(b)　　　　　　　　(c)

Figure 4. Measurement of (a) Water sorptivity coefficient, (b) Rapid chloride permeability, and (c) Apparent gas permeability.

24 hours. As seen in Figure 5, freeze-thaw cycles were carried out in 6.5 hours, with the temperature decreasing from 4 °C to -18 °C and increasing from -18 °C back to 4 °C. On the other hand, 14 days after manufacturing, three samples with a span length of 344.8 were tested under the four-point bending test up to failure, and the average mid-span beam deflection capacity and ultimate flexural strength were calculated. These results were used as control to base the pre-cycle flexural performance of the samples.

At the end of every of 50 freeze-thaw cycles, the samples were taken out of the cabinet. After being kept for 1 day, they were photographed and weighed, and the ultrasonic pulse velocity (UPV) values were measured. UPV measures the time of the first arrival of an ultrasonic wave from one side of the sample to another. The test result of UPV assesses the relative quality of concrete or geopolymer in the presence of imperfections (i.e., voids, cracks, and the effectiveness of its repairs). Then, the samples were put back into the freeze-thaw cabinet. Each time, the chambers were cleaned and filled with fresh water. All of the EGCs completed 300 cycles and were subjected to the four-point bending test, their residual bending performances were found, and flexural strength-mid-span beam deflection graphs were obtained. Furthermore, after the samples' flexural performance was measured, the crack numbers and widths were determined with the help of a handheld microscope.

After 300 freeze-thaw cycles, the relative dynamic modulus of elasticity (RDME) of EGCs was determined with the formulae below. The first formula proposed to find P_c is given in Equation [3].

$$P_c = (n_1^2 / n^2)x100 \qquad [3]$$

P_c: relative dynamic modulus of elasticity after freeze-thaw cycles, n: 0 is the fundamental transverse frequency in the freeze-thaw cycle, and n_1: c is the fundamental transverse frequency in the freeze-thaw cycle. Although not explained in ASTM C666 (2015), RDME, which uses UPV measurements instead of basic transverse frequency values, can also be calculated using Equation [4] (57).
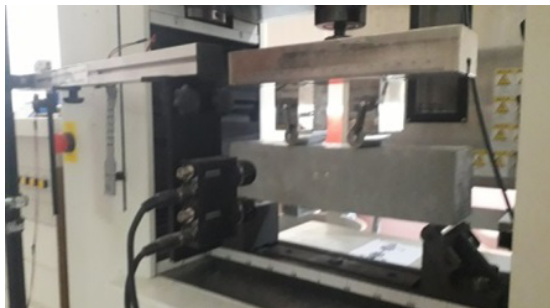
$$P_c = (v_c^2 / v_0^2)x100 \qquad [4]$$

P_c: c is the relative dynamic modulus of elasticity after freeze-thaw cycles, v_0: 0 is the UPV value in the freeze-thaw cycle, and v_c: c is the UPV value in the freeze-thaw cycle. Equation [4] was used to determine the RDME in the present study.

2.8. Drying shrinkage

For each EGC mix, three 285x25x25 mm bar samples were cast to monitor the drying shrinkage and
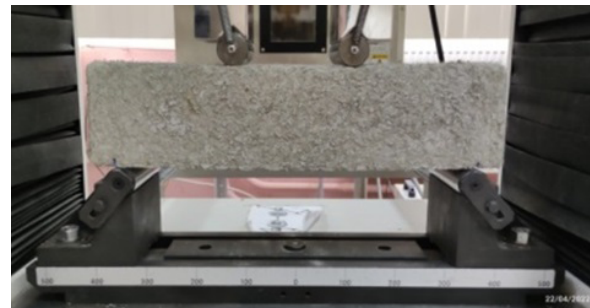

(a)

(b)

Figure 5. (a) The samples' images at -18 °C and +4 °C, (b) Determination of flexural performance of EGCs at day 14 and after 300 FTCs.

the mass loss (180 days after the initial curing of 1 day in the mold and 27 days in own cure (in water at 60 °C) according to ASTM C157) (58). As seen in Figure 6(a), the samples were then kept at 50±5% RH and 23±2 °C in an environmental chamber. During this period, the weights and length changes (Figure 6(b)) of the samples were determined on certain days.
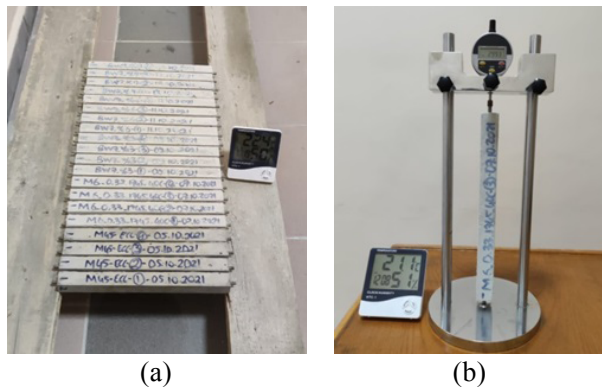

FIGURE 6. (a) Keeping the samples in the special curing room, (b) Performing the length measurements.

2.9. Microstructural analysis

The microstructural properties of EGCs were determined with the help of samples obtained from matrices. TGA/DTA analysis was applied to SWM0, SWM6, and SWM9 mixes. TGA analysis was carried out on 15 mg powder samples in the temperature range of 25–1000 °C, under nitrogen atmosphere conditions with a scanning speed of 10 °C/min. DTA curves were drawn with the obtained data after this analysis.

3. RESULTS AND DISCUSSION

3.1. Mini-slump flow diameter

Table 4 shows the average slump diameters of each mix. It is known that PVA fiber can significantly reduce the slump flow of EGC depending on the increased friction value between fibers and between the matrix and fibers, in addition to the decreased packing density (59, 60). As a result of a lot of trial and error, EGCs, with/without PVA fiber, were produced with slump flow diameters very close to each other. In other words, the slump flow diameters of EGCs with/without PVA fiber ranged from 16.4±0.2 cm to 32.4±0.2 cm, respectively. To this end, as seen in Table 3, SWM9, SWM6, and SWM3 mixes could be produced with 34%, 7%, and 3% higher water content than SWM0 mix, respectively. Therefore, it can be said that for both EGCs with/without PVA fiber, workability decreased with the increasing SWM content. It is known that FA has a smooth surface and spherical particle structure. Thus,

TABLE 4. Mini-slump flow diameter of EGCs.

Fresh Properties	SWM0	SWM3	SWM6	SWM9
Flow Diameter without PVA (cm)	32.6	32.1	32.4	32.5
Flow Diameter with PVA (cm)	16.6	16.1	16.5	16.5

FA increases the workability of EGCs (6). Unlike FA, the acicularity of SWM can form network structures by overlapping between each other, which results in the decreased workability of mixes (40, 61). Thus, the probability of such network structures increases with the increasing amount of SWM due to the interlocking of SWM needles (23, 35, 62). Moreover, this can be identified as a result of the interlocking of SWMs due to the acicular particle structure (6, 38). Nevertheless, it should be noted that water only improves the workability of EGCs and does not take part in the geopolymerization reactions different from the chemical reaction of cementitious composites (63). In other words, the role and existence form of water in the geopolymer are related to the way of geopolymerization. Qualitative analysis indicates that water is released during the reaction (64). The evaporated water leaves discontinuous nanopores, improving the performance of the geopolymer. Thus, water plays no role in chemical reaction processes but simply enhances the mixture's workability during production. This differs from the hydration of cementitious composites, where water is involved in a chemical reaction (63).

3.2. Compressive strength

Figure 7 represents the compressive strength values of cubes for EGCs with/without PVA fiber at 7 and 28 days. Low-calcium systems, such as FA-based ones, tend to generate an alkali alumino-silicate (N–A–S–H) gel with a highly crosslinked (mainly Q^4), disordered pseudo-zeolitic structure. When GGBFS (high calcium precursor) is additionally used, C-A-S-H gel with a tobermorite-like structure is another reaction product (65, 66). These gels can coexist in binders based on blends of high-calcium and low-calcium precursors (65), although the stability of the gel coexistence at high alkalinity is still the subject of discussion (65). Garcia-Lodeiro et al. (67) found a tendency toward C–A–S–H gel as the final stable product when pH remained > 12 in mixtures of synthetic C–S–H and N–A–S–H gels. In other words, GGBFS used together with FA in the geopolymerization process indicated that the increase in strength performance was mostly provided by GGBFS with higher reactivity, the development of the microstructure, and the gel phase of geopolymers. GGBFS is the basic precursor of alkaline activation for FA+GGBFS-based geopoly-

mers at ambient curing (68). Additionally, geopolymers with GGBFS can reach considerably higher strength with oven curing. However, the material has a cracking problem (27). The geopolymer containing GGBFS, which is heated under the effect of temperature, expands just like concrete. While composites such as concrete or geopolymer containing GGBFS, which start to dry from the surface, dry normally, since the inner part does not interact with air, it starts to dry later and expand from the inside due to the effect of temperature. This causes such composites to exert outward pressure. However, since the surface of the concrete or geopolymer containing GGBFS has already dried, it is subjected to pressure from the inside. The concrete or GGBFS containing geopolymer shell, which is dry on the outside, starts to crack, and these cracks cannot be reversed. To prevent this, the concrete is frequently irrigated, especially in hot weather. This is the main reason for the hot water curing of the FA+GG-BFS-based geopolymer developed in the present study. Therefore, the researchers (27) suggested hot water curing to take advantage of the high strength performance of GGBFS. Thus, high cubes of EGCs with/without PVA fiber varied between 88.1-111.1 and 95.1-122.6 MPa at 7 and 28 days, respectively. The compressive strength of EGCs without PVA fiber, named SWM3, SWM6, and SWM9 mixes, was 6.3%, 12.1%, and 1.9% higher than that of SWM0, respectively, whereas SWM3, SWM6, and SWM9 mixes incorporating PVA fiber had 4.6%, 11.5%, and 1.2% higher compressive strength than that of SWM0 at 7 days, respectively. In comparison with SWM0 at 28 days, the increment ratio of compressive strength was determined as 6.5%, 11.2%, 2.6%, 6.7%, 11.0%, 4.0% for SWM3, SWM6, and SWM9 with/without PVA fiber, respectively. As seen in Figure 7, the addition of PVA fiber reduced bulk density by increasing flaws and interfaces in the geopolymer paste, thus decreasing the compressive strength of EGCs (69, 70). The replacement ratio of SWM has more impact on the compressive strength of EGCs. In other words, the highest compressive strength was observed in SWM6. This may be explained by the improving effects of SWM, which is used instead of FA in the geopolymer matrix, explained by the fibrous structure due to the acicular particle morphology of SWM (71). It can also be said that SWM, with the feature of bridging microcracks due to its fibrous structure, enhanced bond strength between the matrix/microfiber at the interface of EGCs (72). As seen in Figure 3 the grain size distribution of SWM was higher than that of FA, and, therefore, SWM may have increased the pore volume of EGCs. However, it is known that the pore discontinuity in the matrix provided by wollastonite occurs due to its needle-like particle structure. The main reason for this discontinuity is that wollastonite forms a pore structure where liquids cannot
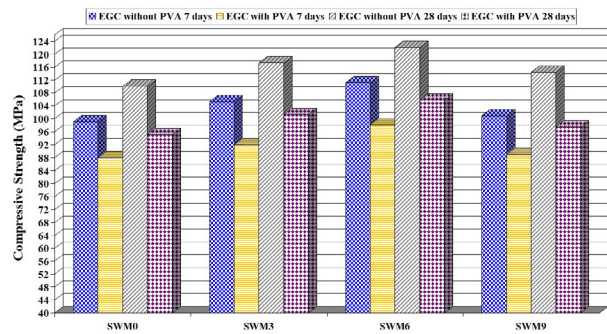

Figure 7. Compressive strength values of EGCs.

reach normal pressure. Furthermore, the presence of SWM in the pore system, which has no chemical effect on the pore solution due to its inert nature, is thought to affect the formality of the pore network folds of ECC with its needle-like particle structure (38, 41). This agrees with the studies by Öz and Güneş (38) and Yücel et al. (6), showing that the mechanical performance of the cementitious composite developed with 9% SWM decreased beyond this substitution level. Likewise, there was a decreasing trend with the usage of 9% SWM in EGCs, although SWM9 with/without PVA fiber has a higher strength than that of SWM0. The excessive amount of SWM in the geopolymer matrix was the reason for the decreased compressive strength since workability loss originated from the high surface area of SWM for the desired slump flow diameter of FA+GGBFS-based EGCs (41). This information was accepted by Patankar et al. (72), indicating that the excessive amount of water for geopolymerization did not have any positive effect on the strength properties of geopolymers. It was also noted that the parameters defined as fiber dispersion in the paste and the type and amount of fiber had a significant effect on the interaction between the matrix and fiber. Hence, the large amount of SWM with inert characteristics no longer contributed to the improvement of the compressive strength for FA+GG-BFS-based EGCs (11).

3.3. Water Sorptivity Coefficient

Figure 8 presents the water sorptivity coefficient of FA+GGBFS-based EGCs with PVA and SWM. The 7-day and 28-day water sorptivity coefficients were in the range of 0.1706-0.2071 and 0.1089-0.1251 mm/min$^{0.5}$ for FA+GGBFS-based EGCs, respectively. The water sorptivity coefficients of SWM3, SWM6, and SWM9 mixes were 7.8%, 17.6%, and 12.3% lower than that of SWM0 at 7 days, respectively. On the other hand, the improvement ratio of the water sorptivity coefficient in comparison with SWM0 was determined as 5.9%, 13%, and 7% for SWM3, SWM6, and SWM9 at 28
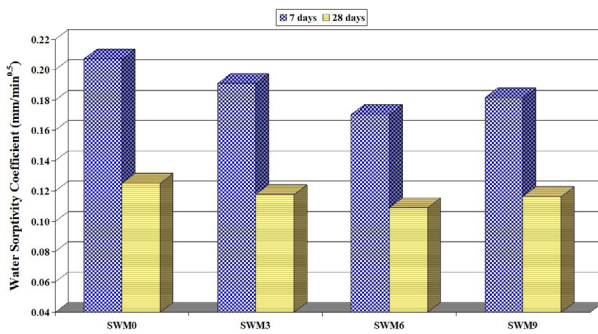
Figure 8. Water sorptivity coefficients of EGCs.

days, respectively. Similar to the current study, Mathur et al. (73) stated that wollastonite microfibers reduced the water absorption amount of cementitious composites. Thus, it can be concluded that the lowest water sorptivity coefficient among FA+GG-BFS-based EGC mixes was obtained from SWM6 mix, while SWM0 had the highest water sorptivity coefficient. As a result, it can be thought that SWM enhanced the compactness of the microstructure in the EGC matrix (73-75). Hence, a pore discontinuity could be ensured with the pore structure formation of SWM in the matrix, which liquids cannot reach at normal pressures (41, 73). Moreover, using SWM at a 9% replacement level deteriorated the permeability performance of SWM9 with respect to SWM6. The high amount of SWM in EGCs was the reason for the weakened matrix bond in the interfacial transition zone (33). As a result, the pores created by the high amount of SWM resulted in the increased water sorptivity coefficients of EGCs.

3.4. Rapid Chloride Permeability

The chloride permeability values of EGCs at 7 and 28 days are graphically shown in Figure 9. The rapid chloride permeability coefficients of FA+GG-BFS-based EGCs changed between 4412-5011 and 3055-3483 at 7 and 28 days, respectively. The total charge passing through FA+GGBFS-based EGCs,
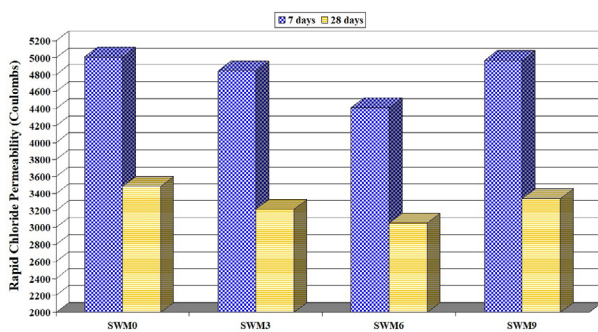
including SWM, was in the range of 2000-4000 C at 28 days, thus leading to the moderate classification of rapid chloride permeability in accordance with ASTM C 1202 (54). In the development of EGCs, the substitution percentage of SWM had a significant effect during the activation process, in addition to the constant parameters such as the alkali activator ratio and curing temperature. Thus, the highest rapid chloride permeability coefficient was obtained from SWM0, while SWM6 had the lowest one. The studies by Ransinchung et al. (75), Kalla et al. (74), and Kumar and Ramujee (71) also supported this result. The pore discontinuity provided by SWM, with its needle-like particle morphology, can be considered the main reason for this improvement (73). Owing to its inert structure, SWM does not enter any chemical reaction with the pore solution, which preserves its physical structure during geopolymerization. Therefore, the unique structure of SWM may affect the formality of the pore network folds of EGCs. It can also be said that the bridging capacity in the pore structure provided by SWM positively affects the pore network folds against the rapid chlorine permeability (38). However, the high replacement ratio of SWM9 caused the poor compaction of fresh EGCs. Then, the porous structure formation occurred due to the heterogeneous interaction between SWM and the matrix, which caused the deficiencies of the poor system to result in the increased rapid chloride permeability coefficient.

3.5. Gas Permeability

Figure 10 presents the details of the apparent gas permeability coefficient of EGCs at 7 and 28 days. The lowest gas permeability coefficients among EGCs were obtained for SWM6 as 5.71 x10^{-16} and 4.79 x10^{-16} m^2 at 7 and 28 days, respectively. As expected, the highest gas permeability coefficients at 7 and 28 days were obtained from SWM0 as 6.55 x10^{-16} and 5.75 x10^{-16} m^2, respectively. It is known that the durability properties of geopolymer depend on the microstructural performance of the matrix and the pore structure of the surface (39).
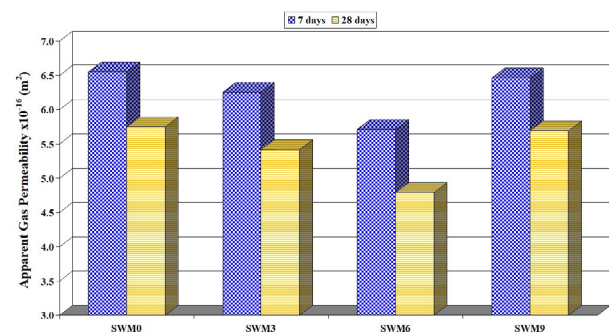

Figure 9. Rapid chloride permeability values of EGCs.

Figure 10. Apparent gas permeability values of EGCs.

From a physicochemical perspective, this may be explained by SWM having good adsorptive properties with the rough surface reducing the water absorption of EGCs by its reinforcing effect (39, 74, 75). Additionally, SWM can become a center of the formation relationship with FA and GGBFS particles of composites, and thus, the "constraint" mobility can continue (76). On the other hand, SWM with acicular particles, bridging ability, and inert structure, which does not have any chemical effect on the pore solution, enhanced the pore network of the material and resulted in pore discontinuity in the geopolymer matrix (74, 75). Despite this result, the poor gas permeability performance of SWM9 in comparison with SWM3 and SWM6 can be attributed to the decreasing paste strength of EGCs in the interfacial transition zone of SWM (33). Consequently, the gaps created by the weakness of the matrix resulted in the deterioration of the gas permeability coefficients for EGCs.

3.6. Freeze-Thaw Resistance

EGCs can deteriorate under various environmental loads (e.g., freeze-thaw cycles). However, it is expected that the permeability of EGCs can be much less in comparison with similarly strained concrete due to its tight crack width, which would be useful for the durability of cementitious composites (4). The effects of SWM amount on the mass change (mass loss) and UPV measurement of FA+GGBFS-based EGCs samples subjected to 50, 100, 150, 200, 250, and 300 freeze-thaw cycles are shown in Figures 11-12, respectively. Moreover, Figure 13
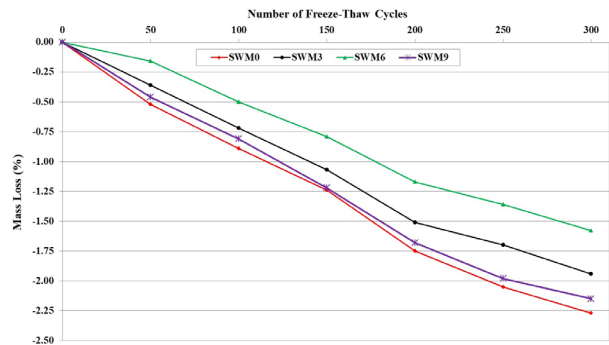

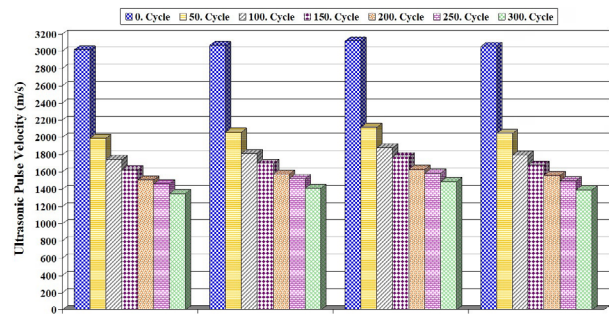**FIGURE 11.** % Mass losses of EGCs during FTCs.

FIGURE 12. UPV variations of EGCs during FTCs.

displays the appearance of SWM6 sample at the end of 0, 50, 150, and 300 freeze-thaw cycles. As a result of freeze-thaw cycles, it was determined that the presence of SWM in the mixtures of FA+GGBFS-based EGCs reduced the mass loss and UPV values. For example, after 300 freeze-thaw cycles, the
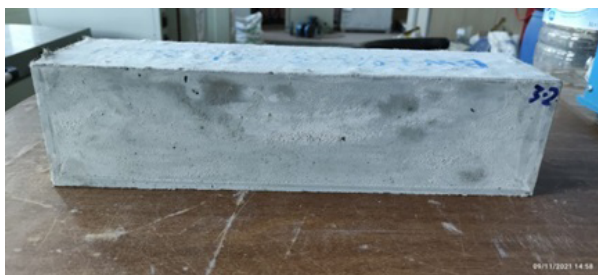
FIGURE 13. Appearance of SWM6 mix at the end of (a) 0, (b) 50, (c) 150, and (d) 300 FTCs.

mass losses of SWM0, SWM3, SWM6, and SWM9 mixes were obtained as 2.27%, 1.94%, 1.58%, and 2.15%, respectively. Likewise, the UPV measurement at the end of 300 freeze-thaw cycles of these mixes decreased by 55.19%, 54.04%, 52.23%, and 54.41%, respectively. SWM used instead of FA partially increased the void ratio of EGCs due to its larger grain size than that of FA. However, the increase in UPV measurement for SWM3, SWM6, and SWM9 with respect to SWM0 was considered evidence that SWM provided pore discontinuity in the matrix (33, 72, 73). On the other hand, an increase in the durability of EGCs can be related to the reduced permeability of the matrix system due to the formation of discontinuous pores. Furthermore, the increased porosity of the matrix with the use of SWM up to a 6% replacement level with FA is likely to accommodate frozen water (ice) without stress formation in EGC. Therefore, the array of interactions within the composite matrix, including SWM, led to the unique pore size distribution, resulting in a composite capable of resisting freeze-thaw (73). Moreover, the downward durability trend for UPV measurement and mass loss of SWM9 may be explained by the limited geopolymerization with excess SWM.

Figure 14 shows the variations of the relative dynamic modulus of elasticity (RDME) values depending on the number of freeze-thaw cycles. For all freeze-thaw cycles in every 50 cycles, the lowest RDME values were obtained from SWM0. It was determined that SWM6 performed the best in terms of RDME. Unfortunately, the durability factor (DF) value of all FA+GGBFS-based EGCs at the end of the 50th cycle was obtained as "60" smaller than the value specified in the ASTM C666 standard (56). Therefore, the DF values of EGCs were determined as 0.

Mid-span beam deflection and flexural strength values and curves of EGCs at the end of 14 days and 300 freeze-thaw cycles are presented in Figures 15-17, respectively. According to the results, it is not difficult to state that the flexural strength of geopolymer samples is related to compressive strength. As seen in Figures 15-17, the mid-span beam deflection and flexural strength values of EGCs increased
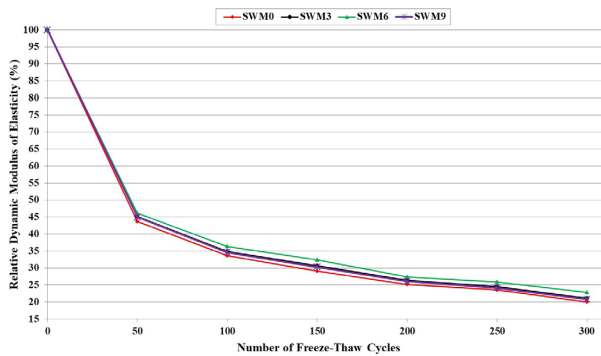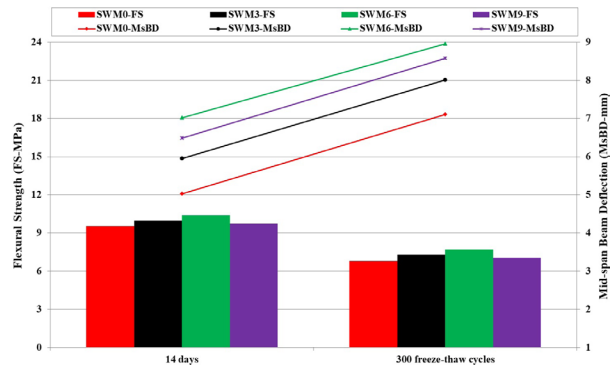

Figure 15. Flexural strengths and mid-span beam deflections of EGCs at 14 days (0th cycle) and at the end of 300 FTCs.
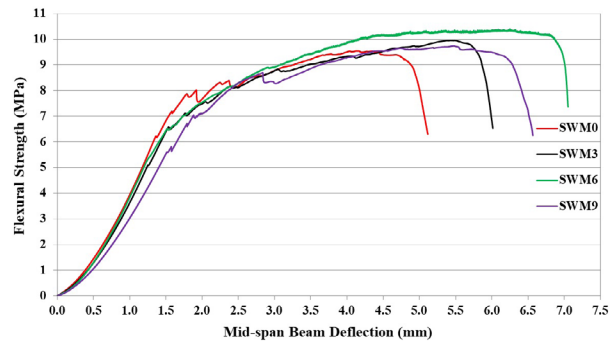

Figure 16. Flexural strength and mid-span beam deflection curves of EGCs at 14 days (0th cycle).
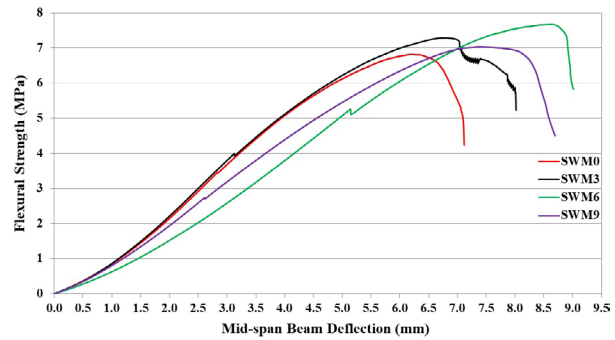

Figure 17. Flexural strength and mid-span beam deflection curves of EGCs at the end of 300 FTCs.

up to a 6% SWM replacement level, while SWM9 had lower mid-span beam deflection and flexural strength values than those of SWM6 but higher than those of SWM0. The mid-span deflections of SWM3, SWM6, and SWM9 increased by approximately 18.3%, 39.6%, and 28.8%, respectively, compared to SWM0 for 14 days. The flexural strength values were determined as 4.3%, 8.9%, and 2.0%, respectively. As predicted, the flexural strength of all EGCs decreased due to the damage at the end of 300 freeze-thaw cycles. This trend reached quite high values for EGCs. However, the ductility capacity of FA+GG-

Figure 14. RDME variations of EGCs during FTCs.

BFS-based EGCs incorporating SWM increased significantly, contrary to expectations. Thus, SWM improved the flexural performance of EGCs up to a 6% content, just as before freeze-thaw cycles. The mid-span deflections of SWM3, SWM6, and SWM9 mixes increased by approximately 12.7%, 25.6%, and 20.5%, respectively, with respect to SWM0 after 300 freeze-thaw cycles. The flexural strength values were determined as 6.9%, 12.6%, and 3.2%, respectively. The bridging ability of SWM improved the resistance of EGCs during freeze-thaw cycles, resulting in higher flexural performance of FA+GG-BFS-based EGCs. It is also evident from Figures 16 and 17 that the acicular structure of SWM ensures bridging the micro-cracks of FA+GGBFS-based EGCs (39). However, a higher content of SWM in SWM9 ensures no further improvement in flexural strength. Hence, the lacking interfacial adhesion of SWM and EGC paste reduced the flexural strength at the end of 300 freeze-thaw cycles (74, 75).

The average crack width and crack number values at the end of the 14th day and 300 freeze-thaw cycles of EGCs are given in Figure 18. It was revealed that the number of cracks changed as the ductility of composites was enhanced by SWM. Likewise, the crack width of EGCs decreased with the increasing ductility.

3.7. Drying Shrinkage

The drying shrinkage and mass loss variations of FA+GGBFS-based EGCs up to 180 days of drying are graphically depicted in Figures 19 and 20, respectively. The drying shrinkage of SWM0 was determined as 2140.44 µε at the end of the 180-day drying period. According to these findings on SWM9, SWM3, and SWM6, the drying shrinkage of FA+GGBFS-based EGCs decreased in the aforesaid order, but all of the EGCs incorporating SWM exhibited lower shrinkage than SWM0. Hence, the lowest drying shrinkage among FA+GGBFS-based EGCs was obtained as 2000.18 µε from SWM6 after the 180-day drying period. Moreover, similar test

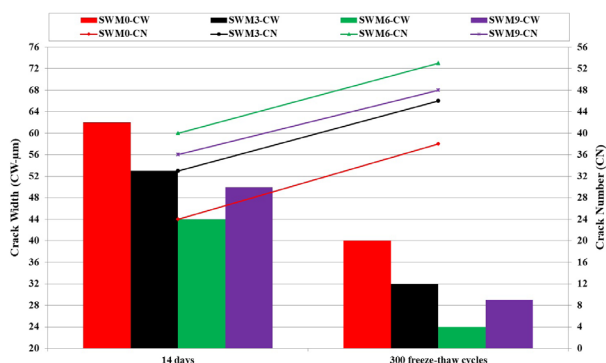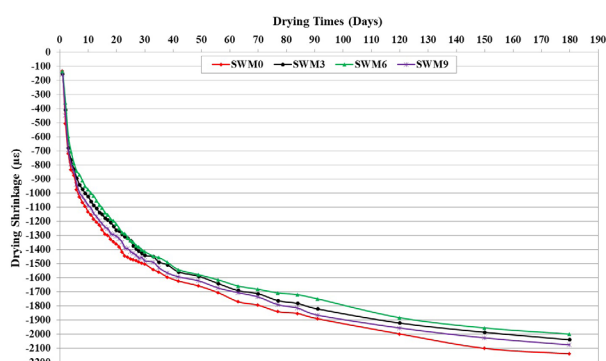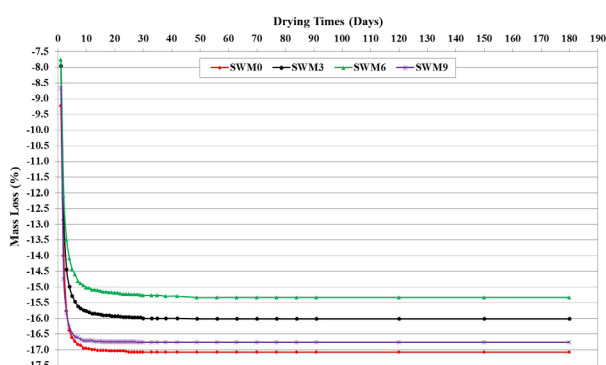**FIGURE 19.** 180-day drying shrinkage variations of EGCs.

FIGURE 20. 180-day % mass loss variations of EGCs.

results to the present study were reported by other studies, indicating that the bridging ability of micro-cracks and contribution to pore discontinuity, as well as the inert characteristics of SWM, were accompanied by lower shrinkage strain in SWM3, SWM6, and SWM9 in comparison with SWM0, as confirmed by the decrease in drying shrinkage with the increasing SWM content in EGCs (35, 72, 77). It can be stated that SWM, with crystal or needle grain forms, has certain roughness forms around itself, associated with surrounding materials, and forms the matrix of the main composites as micro-reinforcing. This reduces the degree of their mobility independently of one another. Therefore, the drying shrinkage of SWM6 was noticeably decreased by SWM with high adhesion (76). As seen in Figure 20, the % mass loss changes of EGCs exhibited similar trends with the drying shrinkage results, especially until the 15th day. While the highest mass loss was obtained from SWM0 as 17.07%, SWM6 had the lowest mass loss of 15.33%. However, after day 15, the drying shrinkage increased steadily despite the fact that the % mass loss remained almost constant for all EGCs. This may be explained by the fact that drying shrinkage deformation is associated with factors other than mass loss (78). Hence, mass loss alone cannot represent sufficient data on the variations of drying shrinkage for FA+GGBFS-based EGCs (79).

FIGURE 18. Crack widths and crack numbers of EGCs at 14 days (0th cycle) and at the end of 300 FTCs.

3.8. TGA/DTA

The TGA/DTA curves of FA+GGBFS-based EGCs are shown in Figures 21-22, respectively. According to previous studies (38, 80), the decrease in water in the N-A-S-H gel for FA-based geopolymers can be attributed to the peak occurring in the 50-150 °C range due to the reduction in mass. Moreover, for alkali-activated GGBFS-based composites, the initial mass loss at 50-200 °C indicates the presence of a C-S-H-like solid phase and dehydration in the geopolymer paste (81, 82). The N-A-S-H and C-S-H gel contents of EGCs were determined by the mass losses determined by the peak temperatures of the TGA curves in the range of 20(initial)-200(final) °C in the DTA graphs. The gel contents of SWM0, SWM6, and SWM9 were calculated as 9.27%, 8.77%, and 7.97%, respectively. The analysis results indicated that the gel contents of EGCs with SWM did not change in parallel with compressive strength. The compressive strength of SWM6 and SWM9 was higher than that of SWM0. The gel content of EGCs gradually decreased with the increasing SWM content. These results showed that SWM was not involved in the reactions between the alkali activator and GGBFS/FA in the chemical reaction zones due to its inert structure (38, 39). It can be stated that its presence in the regions prevented chemical reactions. Moreover, the decrease in FA can be 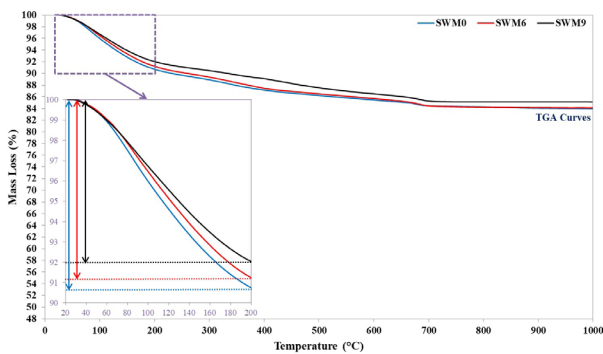thought to be another reason for the decreased to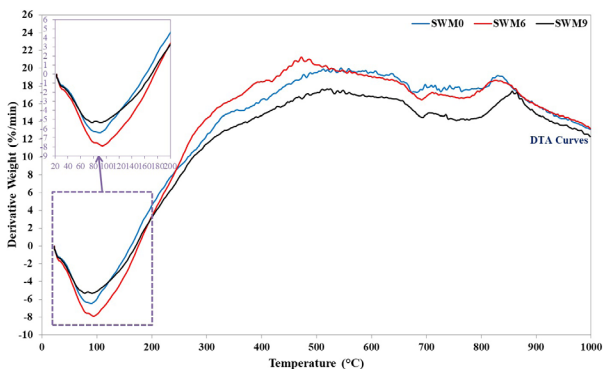tal gel content. Based on the gel contents calculated with the TGA/DTA results and compressive strength values, although the gel contents decreased with SWM, its improving effects on compressive strength can be attributed to its superior physical shapes in the microstructure. Due to its acicular particle structure, SWM can bridge micro-cracks, leading to a higher load-carrying capacity (35, 38, 39). Additionally, the improvement in the durability and dimensional stability performance of EGCs can be explained by the inert characteristics of SWM. In fact, although it is predicted to increase the pore volume, SWM preserves its acicularity by not participating in the chemical reaction, thus providing pore discontinuity with this physical structure (6, 38, 39).

4. CONCLUSIONS

This paper investigated the effects of SWM on the characteristics of FA+GGBFS-based EGCs by experimental methods, including mini slump-flow diameter, compressive strength, water sorptivity coefficient, rapid chloride permeability, apparent gas permeability, freeze-thaw resistance, and drying shrinkage. In this way, the following results can be drawn:

- The mini slump-flow diameters of EGCs with/without PVA fiber ranged from 16.4±0.2 cm to 32.4±0.2 cm, respectively. It is expected that SWM will reduce the workability characteristics of EGCs due to its needle-shaped structure. However, this problem can be compensated by adding water to the geopolymer mixture as the mini slump-flow diameters of EGCs are fixed.
- The highest compressive strength among EGCs with/without PVA fiber was observed as 122.6 MPa in SWM6 at 28 days. This may be explained by the improving effects of SWM, which is used instead of FA in the geopolymer matrix due to its fibrous texture owing to the needle-like structure and bridging ability of SWM displaying inert characteristics at the optimum curing condition, binder content, and alkali activator ratio for EGCs. Likewise, there was an incline trend with the usage of 6 wt% SWM in FA+GGBFS-based EGCs in terms of water sorptivity coefficient, rapid chloride permeability, apparent gas permeability, freeze-thaw resistance, and drying shrinkage test results. Indeed, the ability of SWM to bridge micro-cracks contributed to pore discontinuity, which resulted in the better durability and dimensional stability characteristics of EGCs. However, the poor strength, durability, and dimensional stability performance of SWM9 can be attributed to the weakening of the matrix bond in the interfacial transition zone of SWM in FA+GGBFS-based EGCs.
- The TGA/DTA analysis showed that the gel content decreased with the increasing SWM

FIGURE 21. TGA results of EGCs.

FIGURE 22. DTA results of EGCs.

content. This was interpreted as evidence that SWMs are inert substances and do not participate in chemical reactions. Furthermore, the decrease in gel content led to the thought that SWMs prevented the reaction between the alkali activator and GGBFS and FA as a filler material in the chemical reaction zone. Thus, it preserved the needle-like particle structure, provided pore discontinuity, and positively affected the formality of the pore network folds. Therefore, it improved the durability and dimensional stability performance of EGCs. Moreover, its ability to behave like a fiber increased both its bearing capacity and deformation capacity.

Acknowledgments

Funding sources

Authorship contribution statement

Hatice Öznur Öz: Conceptualization, Data cleansing, Formal analysis, Fund raising, Research, Methodology, Project administration, Resources, Software, Supervision, Validation, Visualization, Write-up - original draft, Write-up - review & editing.

Muhammet Güneş: Conceptualization, Data cleansing, Formal analysis, Fund raising, Research, Methodology, Project administration, Resources, Software, Supervision, Validation, Visualization, Write-up - original draft, Write-up - review & editing.

Declaration of competing interest

The authors of this article declare that they have no financial, professional or personal conflicts of in-terest that could have inappropriately influenced this work.

REFERENCES

1. Humur G, Çevik A. (2022). Effects of hybrid fibers and nanosilica on mechanical and durability properties of lightweight engineered geopolymer composites subjected to cyclic loading and heating–cooling cycles. Constr. Build. Mater. 326**:**126846. https://doi.org/10.1016/j.conbuildmat.2022.126846

2. Ren D, Yan C, Duan P, Zhang Z, Li L, Yan Z. (2017). Durability performances of wollastonite tremolite and basalt fiber reinforced metakaolin geopolymer composites under sulfate and chloride attack. Constr. Build. Mater. https://doi.org/10.1016/j.conbuildmat.2016.12.103.

3. Wang Y, Wang Y, Zhang M. (2021). Effect of sand content on engineering properties of fly ash-slag based strain hardening geopolymer composites. J. Build. Eng. 34:101951. https://doi.org/10.1016/j.jobe.2020.101951.

4. Zhong H, Zhang M. (2023). Engineered geopolymer composites: A state-of-the-art review. Cem. Concr. Compos. 135:104850. https://doi.org/10.1016/j.cemconcomp.2022.104850.

5. Li VC. (2003). On engineered cementitious composites (ECC)- A review of the material and its applications. J. Adv. Concr. Tech. 1(3):215–230.

6. Yücel HE, Öz HÖ, Güneş M, Kaya Y. (2021). Rheological properties strength characteristics and flexural performances of engineered cementitious composites incorporating synthetic wollastonite microfibers with two different high aspect ratios. Constr. Build. Mater. 306:124921. https://doi.org/10.1016/j.conbuildmat.2021.124921.

7. Sakulich A.R, Li V.C. (2011). Nanoscale characterization of engineered cementitious composites (ECC). Cem. Concr. Res. 41(2):169–175. https://doi.org/10.1016/j.cemconres.2010.11.001.

8. Siad H, Lachemi M, Şahmaran M, Mesbah HA, Hossain KMA. (2018). Advanced engineered cementitious composites with combined self-sensing and self-healing functionalities. Constr. Build. Mater. 176:313–322. https://doi.org/10.1016/j.conbuildmat.2018.05.026.

9. Luukkonen T, Abdollahnejad Z, Yliniemi J, Kinnunen P, Illikainen M. (2018). One-part alkali-activated materials: A review. Cem. Concr. Res. 103:21–34. https://doi.org/10.1016/j.cemconres.2017.10.001.

10. Wang S, Li VC. (2007). Engineered cementitious composites with high-volume fly ash. ACI Mater. J. 104(3):233–241. http://doi.org/10.1201/b15883-8.

11. Hemra K, Kobayashi T, Aungkavattana P, Jiemsirilers S. (2021). Enhanced mechanical and thermal properties of fly ash-based geopolymer composites by wollastonite reinforcement. J. Met. Mater. Min. 31(4):13–25. http://doi.org/10.55713/jmmm.v31i4.1230.

12. Liang GW, Li HX, Zhu HJ, Liu TJ, Chen Q, Guo HH. (2021). Reuse of waste glass powder in alkali-activated metakaolin/fly ash pastes: Physical properties reaction kinetics and microstructure. Res. Conser. Recyc. 173:105721. https://doi.org/10.1016/j.resconrec.2021.105721.

13. Xu J, Kang A, Wu Z, Xiao P, Gong Y. (2021). Effect of high-calcium basalt fiber on the workability mechanical properties and microstructure of slag-fly ash geopolymer grouting material. Constr. Build. Mater. 302:124089. https://doi.org/10.1016/j.conbuildmat.2021.124089.

14. Öz HÖ, Yücel HE, Güneş M, Köker TŞ. (2021). Fly-ash-based geopolymer composites incorporating cold-bonded lightweight fly ash aggregates. Constr. Build. Mater. 272:121963. https://doi.org/10.1016/j.conbuildmat.2020.121963.

15. Zhang J, Fu Y, Wang A, Dong B. (2023). Research on the mechanical properties and microstructure of fly ash-based geopolymers modified by molybdenum tailings. Constr. Build. Mater. 385:131530. https://doi.org/10.1016/j.conbuildmat.2023.131530.

16. Hu S, Wang H, Zhang G, Ding Q. (2008). Bonding and abrasion resistance of geopolymeric repair material made with steel slag. Cem. Concr. Compos. 30(3):239–244. https://doi.org/10.1016/j.cemconcomp.2007.04.004.

17. Pacheco-Torgal F, Castro-Gomes JP, Jalali S. (2008). Adhesion characterization of tungsten mine waste geopolymeric binder influence of OPC concrete substrate surface treatment. Constr. Build. Mater. 22(3):154–161. https://doi.org/10.1016/j.conbuildmat.2006.10.005.

18. Samal S Phan TN, Petríková I, Marvalová B, Vallons KAM, Lomov SV. (2015). Correlation of microstructure and mechanical properties of various fabric reinforced geo-polymer composites after exposure to elevated temperature. Cer. Int. 41(9 Part B):12115–12129. https://doi.org/10.1016/j.ceramint.2015.06.029.

19. Kan Li-li, Wang W-S, Liu W-D, Wu M. (2020). Development and characterization of fly ash based PVA fiber reinforced Engineered Geopolymer Composites incorporating metakaolin. Cem. Concr. Compos. 108:103521. https://doi.org/10.1016/j.cemconcomp.2020.103521.

20. Li W, An J, Lu Y, Li Shan. (2023). Bond stress–slip constitutive relationship between engineered geopolymer composites (EGC). and rebar under cyclic loading. Constr. Build. Mater. 409:133998. https://doi.org/10.1016/j.conbuildmat.2023.133998.

21. Ohno M, Li VC. (2018). An integrated design method of engineered geopolymer composite. Cem. Concr. Compos. 88:73–85. https://doi.org/10.1016/j.cemconcomp.2018.02.001.

22. Nematollahi B. (2017). Investigation of geopolymer as a sustainable alternative binder for fiber-reinforced strain hardening composites. Ph.D. thesis Swinburne University of Technology.

23. Vickers L, Rickard WDA, Riessen AV. (2014). Strategies to control the high temperature shrinkage of fly ash based geopolymers. Thermo. Acta. 580:20–27. http://doi.org/10.1016/j.tca.2014.01.020.

24. Said SH, Razak H.A, Othman I. (2015). Flexural behavior of engineered cementitious composite (ECC). slabs with polyvinyl alcohol fibers. Constr. Build. Mater. 75:176–188. https://doi.org/10.1016/j.conbuildmat.2014.10.036.

25. Kumar S, Kumar R, Mehrotra SP. (2010). Influence of granulated blast furnace slag on the reaction structure and properties of fly ash based geopolymer. J. Mater. Sci. 45:607–615. http://doi.org/10.1007/s10853-009-3934-5.

26. Buchwald A, Hilbig H, Kaps C. (2007). Alkali-activated metakaolin-slag blends—performance and structure in dependence of their composition. J. Mater. Sci. 42:3024–3032. http://doi.org/10.1007/s10853-006-0525-6.

27. Öz HÖ, Güneş M, Yücel HE. (2023). Rheological and microstructural properties of FA+GGBFS-based engineered geopolymer composites (EGCs). capable of comparing with M45-ECC as mechanical performance. J. Build. Eng. 65:105792. https://doi.org/10.1016/j.jobe.2022.105792.

28. Kuranlı ÖF, Uysal M, Abbas MT, Coşgun T, Nis A, Aygörmez Y, Canpolat O, Al-Mashhadani MM. (2022). Evaluation of slag/fly ash based geopolymer concrete with steel polypropylene and polyamide fibers. Constr. Build. Mater. 325:126747. https://doi.org/10.1016/j.conbuildmat.2022.126747.

29. Temuujin J, Van Riessen A, Williams R. (2009). Influence of calcium compounds on the mechanical properties of fly ash geopolymer pastes. J. Hazar. Mater. 167(1–3):82–88. https://doi.org/10.1016/j.jhazmat.2008.12.121.

30. Coppola L, Coffetti D, Crotti E, Aversano RD, Gazzaniga G. (2019). The influence of heat and steam curing on the properties of one-part fly ash/slag alkali activated materials: Preliminary results. AIP Conf. Proceed. 2196:020038. https://doi.org/10.1063/1.5140311.

31. Nurjaya DM, Astutiningsih S, Zulfia A. (2015). Thermal effect on flexural strength of geopolymer matrix composite with alumina and wollastonite as fillers. Int. J. Tech. 3:462–470.

32. Hemalatha P, Ramujee K. (2021). Influence of nano material (TiO_2). on self compacting Geo polymer concrete containing fly ash GGBS and wollastonite. Mater. Today: Proceed. 43(2):2438–2442. https://doi.org/10.1016/j.matpr.2021.02.279.

33. Wahab MA, Latif IA, Kohail M, Almasry A. (2017). The use of wollastonite to enhance the mechanical properties of mortar mixes. Constr. Build. Mater. 152:304–309. https://doi.org/10.1016/j.conbuildmat.2017.07.005.

34. Archez J, Texier-Mandoki N, Bourbon X, Caron JF, Rossignol S. (2020). Influence of the wollastonite and glass fibers on geopolymer composites workability and mechanical properties. Constr. Build. Mater. 257:119511. https://doi.org/10.1016/j.conbuildmat.2020.119511.

35. Soliman AM, Nehdi ML. (2012). Effect of natural wollastonite microfibers on early-age behavior of UHPC. J. Mater. Civ. Eng. 24(7):816–824. http://doi.org/10.1061/(ASCE)MT.1943-5533.0000473.

36. Silva FJ, Thaumaturgo C. (2003). Fibre reinforcement and fracture response in geopolymeric mortars. Fat. Fract. Eng. Mater. Struct. 26:167–172.

37. Silva FJ, Mathias AF, Thaumaturgo C. (1999). Evaluation of the fracture toughness in poly(sialate-siloxo). composite matrix conference paper. Geopolymer 99:97–106.

38. Öz HÖ, Güneş M. (2021). The effects of synthetic wollastonite developed with calcite and quartz on high performance mortars. Struct. Concr. 22(S1):E257–E272. https://doi.org/10.1002/suco.201900520.

39. Yücel HE, Özcan S. (2019). Strength characteristics and microstructural properties of cement mortars incorporating synthetic wollastonite produced with a new technique. Constr. Build. Mater. 223:165–176. https://doi.org/10.1016/j.conbuildmat.2019.06.195.

40. Bong SH, Nematollahi B, Xia M, Nazari A, Sanjayan J. (2020). Properties of one-part geopolymer incorporating wollastonite as partial replacement of geopolymer precursor or sand. Mater. Letters 263:165-176. https://doi.org/10.1016/j.matlet.2019.127236.

41. Öz HÖ, Ünsal D. (2023). Characteristic properties of fly ash-based self-compacting geopolymer mortars with synthetic wollastonite microfiber produced from silica and calcite. Mater. Constr. 73(349):e307. http://doi.org/10.3989/mc.2023.296322.

42. Kong HJ, Bike S, Li VC. (2003). Development of a self-compacting engineered cementitious composite employing electrosteric dispersion/stabilization. Cem. Concr. Compos. 25(3):301–309. http://doi.org/10.1016/S0958-9465(02)00057-4.

43. Li VC, Wang S, Wu C. (2001). Tensile strain-hardening behavior of polyvinyl alcohol engineered cementitious composite (PVA-ECC). ACI Mater. J. 98(6):483–492. http://hdl.handle.net/2027.42/84671.

44. Li VC, Leung CK. (1992). Theory of steady-state and multiple cracking of short random fiber composites. J. Eng. Mech. 118(11):2246–2264.

45. Marshall D, Cox B. (1988). A J-integral method for calculating steady-state matrix cracking stresses in composites. Mech. Mater. 7(2):127–133.

46. Li V.C. (1993). From micromechanics to structural engineering. Dob. Gakkai Ronbunshu.1993(471):1–12.

47. Nematollahi B, Sanjayan J, Qiu J, Yang E-H. (2017). Micromechanics-based investigation of a sustainable ambient temperature cured one-part strain hardening geopolymer composite. Constr. Build. Mater. 131:552–563. https://doi.org/10.1016/j.conbuildmat.2016.11.117.

48. Nematollahi B, Qiu J, Yang E-H, Sanjayan J. (2017). Micromechanics constitutive modelling and optimization of strain hardening geopolymer composite. Ceram. Int. 43(8):5999–6007. https://doi.org/10.1016/j.ceramint.2017.01.138.

49. Zhang S, Li VC, Ye G. (2020). Micromechanics-guided development of a slag/fly ash-based strain-hardening geopolymer composite. Cem. Concr. Compos. 109:103510. https://doi.org/10.1016/j.cemconcomp.2020.103510.

50. Zhang S, Nedeljkovic M, Ghiassi B, Ye G. (2017). A comparative study on deflection-hardening behavior of ductile alkali-activated composite. International Conference on Strain-Hardening Cement-Based Composites Springer. 123–130.

51. Yücel HE, Jashami H, Şahmaran M, Güler M, Yaman İÖ. (2013). Thin ECC overlay systems for rehabilitation of rigid concrete pavements. Mag. Concr. Res. 65(2):108–120.

52. ASTM C109. (2016). Standard test method for compressive strength of hydraulic cement mortars (using 2-in. or (50-mm): cube specimens). ASTM International West Conshohocken PA USA.

53. ASTM C1585-20 (2020). Standard test method for measurement of rate of absorption of water by hydraulic-cement concretes. ASTM International West Conshohocken PA USA.

54. ASTM C1202. (2012). Standard test method for electrical indication of concrete's ability to resist chloride ion penetration. Annual book of ASTM standards.

55. RILEM TC 116-PCD. (1999). Permeability of concrete as a criterion of its durability. Mater. Struct. 32:174–179.

56. ASTM C666. (2015). Standard test method for resistance of concrete to rapid freezing and thawing. Annual book of ASTM standards.

57. Molero M, Aparicio S, Al-Assadi G, Casati MJ, Hernandez MG, Anaya JJ. (2012). Evaluation of freeze–thaw damage in concrete by ultrasonic imaging. NDT & E Int. 52:86–94. http://doi.org/10.1016/j.ndteint.2012.05.004.

58. ASTM C157. (2014). Standard test method for length change of hardened hydraulic-cement mortar and concrete. Annual book of ASTM standards.
59. Khayat KH, Meng W, Vallurupalli K, Teng L. (2019). Rheological properties of ultrahigh-performance concrete — An overview. Cem. Concr. Res. 124:105828. https://doi.org/10.1016/j.cemconres.2019.105828.
60. Ranjbar N, Zhang M. (2020). Fiber-reinforced geopolymer composites: A review. Cem. Concr. Compos. 107:103498. http://doi.org/10.1016/j.cemconcomp.2019.103498.
61. Cao M, Xu L, Zhang C. (2016). Rheology fiber distribution and mechanical properties of calcium carbonate ($CaCO_3$). whisker reinforced cement mortar. Compos. Part A: App. Sci. Manufact. 90:662–669. https://doi.org/10.1016/j.compositesa.2016.08.033.
62. Archez J, Texier-Mandoki N, Bourbon X, Caron JF, Rossignol S. (2020). Adaptation of the geopolymer composite formulation binder to the shaping process. Mater. Today Commun. 25:101501. https://doi.org/10.1016/j.mtcomm.2020.101501.
63. Zhang P, Gao Z, Wang J, Guo J, Hu S, Ling Y. (2020). Properties of fresh and hardened fly ash/slag based geopolymer concrete: A review. J. Clean. Product. 270:122389. https://doi.org/10.1016/j.jclepro.2020.122389.
64. Hardjito D, Wallah SE, Sumajouw DM, Rangan BV. (2005). Fly ash-based geopolymer concrete. Aust. J. Struct. Eng. 6:77–86.
65. Provis J.L, Palomo A, Shi C. (2015). Advances in understanding alkali-activated materials. Cem. Concr. Res. 78(Part A):110–125. https://doi.org/10.1016/j.cemconres.2015.04.013.
66. Yip CK, Lukey GC, Van Deventer JSJ, (2005). The coexistence of geopolymeric gel and calcium silicate hydrate at the early stage of alkaline activation. Cem. Concr. Res. 35(9):1688–1697. https://doi.org/10.1016/j.cemconres.2004.10.042.
67. García-Lodeiro I, Palomo A, Fernández-Jiménez A, Macphee DE. (2011). Compatibility studies between N–A–S–H and C–A–S–H gels. Study in the ternary diagram Na_2O–CaO–Al_2O_3–SiO_2–H_2O. Cem. Concr. Res. 41:923–931. https://doi.org/10.1016/j.cemconres.2011.05.006.
68. Ling Y, Wang K, Li W, Shi G, Lu P. (2019). Effect of slag on the mechanical properties and bond strength of fly ash-based engineered geopolymer composites. Compos. Part B: Eng. 164:747–757. https://doi.org/10.1016/j.compositesb.2019.01.092.
69. Cai J, Pan J, Han J, Lin Y, Sheng Z. (2022). Low-energy impact behavior of ambient cured engineered geopolymer composites. Ceram. Int. 48(7):9378–9389. https://doi.org/10.1016/j.ceramint.2021.12.133.
70. Zhou J, Pan J, Leung CK. (2015). Mechanical behavior of fiber-reinforced engineered cementitious composites in uniaxial compression. J. Mater. Civ. Eng. 27(1):04014111. http://doi.org/10.1061/(ASCE)MT.1943-5533.0001034.
71. Kumar JB, Ramujee K. (2017). Mechanical & durability characteristics of wollastonite based cement concrete. J. Civ. Eng. 7(1):1-7. http://doi.org/10.26634/jce.7.1.10363.
72. Patankar SV, Jamkar SS, Ghugal YM. (2012). Effect of sodium hydroxide on flow and strength of fly ash based geopolymer mortar. J. Struct. Eng. 39(1):7–12.
73. Mathur R, Misra AK, Goel P. (2007). Influence of wollastonite on mechanical properties of concrete. J. Scient. Indust. Res. 66:1029–1034.
74. Kalla P, Rana A, Chad YB, Misra A, Csetenyi L. (2015). Durability studies on concrete containing wollastonite. J. Clean. Product. 87:726–734. https://doi.org/10.1016/j.jclepro.2014.10.038.
75. Ransinchung GD, Kumar B, Kumar V. (2009). Assessment of water absorption and chloride ion penetration of pavement quality concrete admixed with wollastonite and microsilica. Constr. Build. Mater. 23(2):1168–1177. https://doi.org/10.1016/j.conbuildmat.2008.06.011.
76. Ibragim U, Erkin E, Aziza K. (2021). Physical properties of high performance concrete on base wollastonite. Europ. J. Life Saf. Stab. 11:101–105. Retrieved from http://ejlss.indexedresearch.org/index.php/ejlss/article/view/203.
77. He Z, Shen A, Lyu Z, Li Y, Wu H, Wang W. (2020). Effect of wollastonite microfibers as cement replacement on the properties of cementitious composites: A review. Constr. Build. Mater. 261:119920. https://doi.org/10.1016/j.conbuildmat.2020.119920.
78. Gesoğlu M, Özturan T, Güneyisi E. (2004). Shrinkage cracking of lightweight concrete made with cold-bonded fly ash aggregates. Cem. Concr. Res. 34(7):1121–1130. https://doi.org/10.1016/j.cemconres.2003.11.024.
79. Güneyisi E, Gesoğlu M, Azez OA, Öz HÖ. (2015). Physico-mechanical properties of self-compacting concrete containing treated cold-bonded fly ash lightweight aggregates and SiO_2 nano-particles. Constr. Build. Mater. 101(1):1142–1153. https://doi.org/10.1016/j.conbuildmat.2015.10.117.
80. Sivasakthi M, Jeyalakshmi R, Rajamane NP, Jose R. (2018). Thermal and structural micro analysis of micro silica blended fly ash based geopolymer composites. J. Non-Cryst. Solids. 499:117–130. https://doi.org/10.1016/j.jnoncrysol.2018.07.027.
81. Ben Haha M, Lothenbach B, Le Saout G, Winnefeld F. (2011). Influence of slag chemistry on the hydration of alkali-activated blast-furnace slag — Part I: effect of MgO. Cem. Concr. Res. 41(9):955–963. https://doi.org/10.1016/j.cemconres.2011.05.002.
82. Lothenbach B, Gruskovnjak A. (2007). Hydration of alkali-activated slag: thermodynamic modelling. Adv. Cem. Res. 19:81–92.